# Electron cyclotron drift instability and anomalous transport: two-fluid moment theory and modeling

Liang Wang\*
Princeton Plasma Physics Laboratory, Princeton, New Jersey 08544, USA and
Department of Astrophysical Sciences, Princeton,
University, Princeton New Jersey 08544, USA

Ammar Hakim and James Juno
Princeton Plasma Physics Laboratory, Princeton New Jersey 08544, USA

Bhuvana Srinivasan

Department of Aerospace and Ocean Engineering,

Virginia Tech. Blacksburg, Virginia 24060, USA

In the presence of a strong electric field perpendicular to the magnetic field, the electron crossfield (E × B) flow relative to the unmagnetized ions can cause the so-called Electron Cyclotron Drift Instability (ECDI) due to resonances of the ion acoustic mode and the electron cyclotron harmonics. This occurs in, for example, collisionless shock ramps in space, and in  $E \times B$  discharge devices such as Hall thrusters. A prominent feature of ECDI is its capability to induce an electron flow parallel to the background E field at a speed greatly exceeding predictions by classical collision theory. Such anomalous transport is important due to its role in particle thermalization at space shocks, and in causing plasma flows towards the walls of E × B devices, leading to unfavorable erosion and performance degradation, etc. The development of ECDI and anomalous transport is often considered requiring a fully kinetic treatment. In this work, however, we demonstrate that a reduced variant of this instability, and more importantly, the associated anomalous transport, can be treated self-consistently in a collisionless two-fluid framework without any adjustable collision parameter. By treating both electron and ion species on an equal footing, the free energy due to the inter-species velocity shear allows the growth of an anomalous electron flow parallel to the background E field. We will first present linear analyses of the instability in the two-fluid five- and ten-moment models. and compare them against the fully-kinetic theory. At low temperatures, the two-fluid models predict the fastest-growing mode in good agreement with the kinetic result. Also, by including more (>= 10) moments, secondary (and possibly higher) unstable branches can be recovered. The dependence of the instability on ion-to-electron mass ratio, plasma temperature, and background B field strength is also thoroughly explored. We then carry out direct numerical simulations of the cross-field setup using the five-moment model. The development of the instability, as well as the anomalous transport, is confirmed and in excellent agreement with theoretical predictions. The force balance properties are also studied using the five-moment simulation data. This work casts new insights into the nature of ECDI and the associated anomalous transport and demonstrates the potential of the two-fluid moment model in efficient modeling of  $E \times B$  plasmas.

<sup>\*</sup> lwang@pppl.gov

### I. INTRODUCTION

In this work, we present two-fluid (electron and ion) investigations of an electrostatic instability due to the electron  $E \times B$  drift relative to unmagnetized ions initially at rest, with the wavevector perpendicular to the uniform background magnetic field. In the fully kinetic description, this instability is often called the electron cyclotron drift instability (ECDI) due to the coupling between the ion acoustic wave and Doppler-shifted discrete electron cyclotron harmonics.

The research interest of ECDI dates back to the 1970s when Refs. [16–20, 33, 34, 55] presented rather thorough kinetic analyses of this instability, motivated primarily by laboratory observations of enhanced fluctuations in low- $\beta$ , collisionless plasma shocks perpendicular to a background magnetic field. At the shock ramp, a fraction of the incoming ions are reflected by the shock potential, picking up a fast drift relative to the incoming electrons, exciting ECDI and other microinstabilities. More recently, ECDI received revived interest in the Earth's bow shocks due to the common observations of electron Bernstein waves in association with ion acoustic waves [7, 14, 22, 37–39, 53, 54], and was suggested to be a potentially important mechanism to allow efficient electron bulk thermalization [11, 54].

ECDI attracted significantly more attention in the Hall effect thruster (HET) research community, stimulated by the continuing efforts to develop electrically powered spacecraft propulsion [6, 13, 21]. In the HET design, a strong electric potential is applied between the anode at the closed end of an annular ceramic channel, and a cathode external to the open end of the channel. Propellant injected at the anode end are ionized by electrons streaming from cathode and accelerated by the applied electric field to produce thrust. To reduce the electron's axial mobility towards the anode and prolong their residency time in the working channel, a radial magnetic field is applied to magnetize the electrons and confine them through the drift in the E × B azimuthal direction. In numerous studies, however, enhanced electron axial (that is, parallel to the applied electric field) mobility is observed that cannot be explained by classical diffusion due to electron-neutral or electron-ion collisions. A number of explanations have since been proposed to understand this anomalous electron transport [6, 47], with the most promising one being an azimuthal instability, which is the topic of this manuscript, the ECDI.

The role of ECDI in the HET context has been actively studied through laboratory experiments and fully kinetic Particle-in-Cell modeling, which could be computationally challenging for full-device studies. Existing fluid and hybrid (fluid-electrons-kinetic-ions/neutrals) modeling efforts have also been successful in producing useful HET operation results, but primarily rely on adjustable parameters, for instance, an adjustable, anomalous collision frequency, to reproduce the observed ECDI characteristics and anomalous electron transport. The conjecture that the enhanced mobility does not manifest self-consistently in a fluid or hybrid framework, is often implied. Thorough reviews on the HETs and the numerical efforts to model their physics to different levels of complexity, including ECDI and anomalous drift, can be found in [6, 21, 26, 47].

In this work, we show how the  $E \times B$  electron drift induce an azimuthal instability in a warm two-fluid (electron-ion) high-moment description without any adjustable parameters, and further, leads to anomalous axial transport of the electrons. This model treats all species, critically, the electrons, in the same manner by evolving their velocity moments, namely number density, velocity, and pressure (and possibly more). The development of an azimuthal instability in this framework is not surprising, due to the free energy available from the velocity difference between electrons and ions. In the cold plasma limit, it reduces to the magnetized Buneman instability [8, 28, 45], therefore the instability itself is not a new finding of this manuscript. The generation of axial transport due to this instability is less evident, though, but can be shown to be a natural result of the Lorentz force applied on the electrons, and, as we will show, is implied by the eigenstructure of the  $E \times B$  instability. We shall also see that, somewhat similar to the fully kinetic description, this instability is due to the coupling between the ion acoustic mode and the Doppler-shifted hybrid wave where the electron cyclotron dynamics play a critical role. However, with only the lower-order velocity moments taken into account, effects due to higher cyclotron harmonics are lost, leading to less or no quantization and consequently greater deviation from a fully kinetic description as the plasma temperature increases.

In this manuscript, we do not intend to suggest the 5-moment two-fluid model as a replacement for the fully-kinetic model, nor to report the discovery of a new fluid instability. Instead, the goals of this paper include (1) to suggest the growth of anomalous transport in a purely fluid description without any collision, which was previously thought to mandate kinetic treatment or anomalous transport; (2) to explore the nature and scaling of the electron drift instability in a finite-temperature two-fluid 5-moment (scalar pressure) plasma; (3) to explore regimes when the fluid and kinetic prediction make a meaningful (not perfect), order-of-magnitude agreement; (4) to show that with more velocity moments included in this two-fluid, high-moment framework, the model may capture higher electron cyclotron harmonics and unstable branches, which helps the model to achieve better agreement with the fully-kinetic treatment at higher temperatures.

This manuscript is outlined as follows. In Section. II, we present the two-fluid high-moment model framework and the linear theory of the ECDI in the 5-moment model, which assumes adiabatic Maxwellian plasma species, as well as some results using the 10-moment model which captures more kinetic physics through higher-order moments. In Section. III, we perform two-fluid 5-moment simulations of the  $E \times B$  configuration and demonstrate the development of ECDI and anomalous electron transport. In Section IV, we compare 5-moment and fully-kinetic Vlasov-Poisson simulations using experimental parameters to demonstrate the capabilities as well as limitation of the former in capturing ECDI and anomalous current. We conclude in Section. V by summarizing the results and providing future motivation to use high-moment models for cross-field instability studies.

#### II. FLUID LINEAR THEORY

A unique and interesting feature of the ECDI in the fully-kinetic description is the discrete growth rates near wave numbers  $k_m = m\Omega_{ce}/v_{\rm E\times B}$ , where  $\Omega_{ce}$  and  $v_{\rm E\times B}$  are the electron cyclotron frequency and drift velocity, and m is an integer mode numbers. This is evident in the example in Figure 1c, where the green curves represent a typical dispersion relation of ECDI in the fully-kinetic (Vlasov) description. As shown in Figure 1c, the kinetic growth rate of ECDI peaks near integer multiples of  $\Omega_{ce}/v_{\rm E\times B}$  due to the coupling of the ion acoustic wave and Doppler-shifted Bernstein harmonics at integral multiples of  $\Omega_{ce}$ . At lower temperatures, however, the quantized unstable branches expand and eventually form a single unstable interval, as indicated by the growth rates shown in Figure 1(a-b). In this section, we will present linear analysis of the ECDI in the two-fluid 5-moment and 10-moment theories to demonstrate their similarities and differences from a fully-kinetic description in describing the ECDI.

## A. The two-fluid 5-moment and 10-moment models

A key concept in the multifluid high-moment model framework is the equal treatment of all populations in the plasma, critically, the electrons. In other words, the electron flows, inertial, and thermal effects are self-consistently evolved instead of inferred from assumptions like quasi-neutrality, etc. In this work, we focus on the 5-moment model in this framework, which assumes the electron and ion pressures to be isotropic, i.e., scalars [23],

$$\frac{\partial \rho_{s}}{\partial t} + \nabla \cdot (\rho_{s} \mathbf{v}_{s}) = 0, 
\frac{\partial (\rho_{s} \mathbf{v}_{s})}{\partial t} + \nabla p + \nabla \cdot (\rho_{s} \mathbf{v}_{s} \mathbf{v}_{s}) = n_{s} q_{s} (\mathbf{E} + \mathbf{v}_{s} \times \mathbf{B}), 
\frac{\partial \mathcal{E}_{s}}{\partial t} + \nabla \cdot [\mathbf{v}_{s} (p_{s} + \mathcal{E}_{s})] = n_{s} q_{s} \mathbf{v}_{s} \cdot \mathbf{E}.$$
(1)

Here,  $\rho_s$ ,  $\mathbf{v}_s$ ,  $p_s$ , and  $\mathcal{E}_s = p_s/\left(\gamma_{\rm gas}-1\right) + \frac{1}{2}\rho_s v_s^2$  are the mass density, velocity, thermal pressure, and total energy of the plasma population s. For electrostatic problems (like ours), the magnetic field is supplied as a background, while the electric field is solved with the Poisson's equation, coupling all plasma populations through their charge densities [23, 52].

In addition to the 5-moment model, in this work, we will also present some results from the 10-moment model where plasma pressures are treated as full tensors with potentially unequal diagonal and

non-vanishing off-diagonal elements [24]:

$$\begin{split} &\frac{\partial n}{\partial t} + \frac{\partial}{\partial x_j} \left( n u_j \right) = 0, \\ &m \frac{\partial \left( n u_i \right)}{\partial t} + \frac{\partial \mathcal{P}_{ij}}{\partial x_i} = n q \left( E_i + \varepsilon_{ijk} u_j B_k \right), \\ &\frac{\partial \mathcal{P}_{ij}}{\partial t} = n q u_{[i} E_{j]} + \frac{q}{m} \varepsilon_{[ikl} \mathcal{P}_{kj]} B_l. \end{split}$$

Here, we have neglected subscripts s for simplicity,  $\mathcal{P}_{ij} = \int d\mathbf{v} m v_i v_j f(\mathbf{v})$  is the stress tensor in the rest frame, the square brackets around indices represent the minimal sum over permutations of free indices needed to yield completely symmetric tensors (for example,  $u_{[i}E_{j]} = u_iE_j + u_jE_i$ ). The 10-moment model retains more kinetic effects resulting in one more electron harmonic which is particularly insightful for the ECDI physics. The 10-moment results will be used to better demonstrate the capability of high-moment models in capturing ECDI, though this paper focuses on the five-moment results primarily.

## B. Dispersion relations in the 5-moment, 10-moment, and fully-kinetic Vlasov models

Consider 1D electrostatic modes in a 1D two-fluid plasma with fully magnetized electrons and unmagnetized ions. The background magnetic field  $\mathbf{B}_0 = B_0 \hat{\mathbf{e}}_z$  is along z and the wavevector  $\mathbf{k} = k \hat{\mathbf{e}}_x$  is along x, perpendicular to  $\mathbf{B}_0$ . There exists a background electric field  $\mathbf{E} = E_0 \hat{\mathbf{e}}_y$  and the fully magnetized electrons flow at the  $\mathbf{E} \times \mathbf{B}$  drift velocity  $\mathbf{v}_{\mathbf{E} \times \mathbf{B}} = \mathbf{E} \times \mathbf{B}/B^2 = v_0 \hat{\mathbf{e}}_x$  along x.

The dispersion relation in the 5-moment regime can be written as

$$1 = \frac{\omega_{pi}^2}{\omega^2 - k^2 c_{si}^2} + \frac{\omega_{pe}^2}{\left(\omega - k v_{\text{EXB}}\right)^2 - k^2 c_{se}^2 - \Omega_{ce}^2},\tag{2}$$

where  $c_{sj} = \sqrt{\gamma p_j/\rho_j}$ ,  $\omega_{pj}$ , and  $\Omega_{cj}$  are the sound speed, plasma and cyclotron frequencies for the species j, respectively. Compared to the well-known cold-plasma Buneman instability, the formal difference here lies in the presence of the electron cyclotron term, i.e., the role of the first electron-electron resonance. Therefore, the name "electron cyclotron drift instability" is still proper for this fluid instability, though the possible quantization due to higher electron cyclotron resonances is missing and leads to greater deviation compared to the fully kinetic counterpart when the plasma temperature goes up. It's worth noting that the existence of drift instabilities in a magnetized two-fluid regime is not surprising, as indicated by Janhunen et al. [28] in the cold plasma limit. However, as we will see, this fluid instability has an important and surprising implication for anomalous transport, an important phenomenon in  $E \times B$  devices. This is what motivates our in-depth investigation of the origin and manifestation of the ECDI in the two-fluid moment model.

As mentioned earlier, the 10-moment model retains the full plasma thermal pressure and one more electron resonance. Its dispersion relation is more complex compared to the 5-moment counterpart and is not given here. Instead, we numerically solve both the 5- and 10-moment dispersion relations using a matrix-based algorithm [24, 51, 56] to find the real and imaginary frequencies for any wavenumber and a set of background physical parameters.

As an example, Figure 1 show the growth rates from electrostatic 5-moment, 10-moment, and Vlasov dispersion relations for parameters used in the Particle-in-Cell benchmark work by Charoy et al.: discharge voltage 200 V, axial length 2.5 cm radial magnetic field B=0.001 T, number density  $n=5\times 10^{16}$  m<sup>-3</sup>, and electron and ion temperatures,  $T_e=1$  eV and  $T_i=0.5$  eV. Though the 5-moment and 10-moment results cannot obtain all the quantized unstable branches that are seen in the kinetic dispersion, the moment models do provide reasonable estimation of fastest growth rate at lower  $T_e$ . It is interesting to note, however, that the 10-moment is able to capture a secondary unstable branch near  $k=\Omega_{ce}/v_{\rm E\times B}$  due to its inclusion of the full pressure tensor. In the future work, one may include even higher velocity moments recover higher electron cyclotron branches, giving better agreement with the Vlasov prediction.

The agreement between 5-moment and Vlasov predictions can be better understood through the scaling laws in panels (e) and (f) of Figure 1 using the parameters above but with varying  $T_e$ . For these

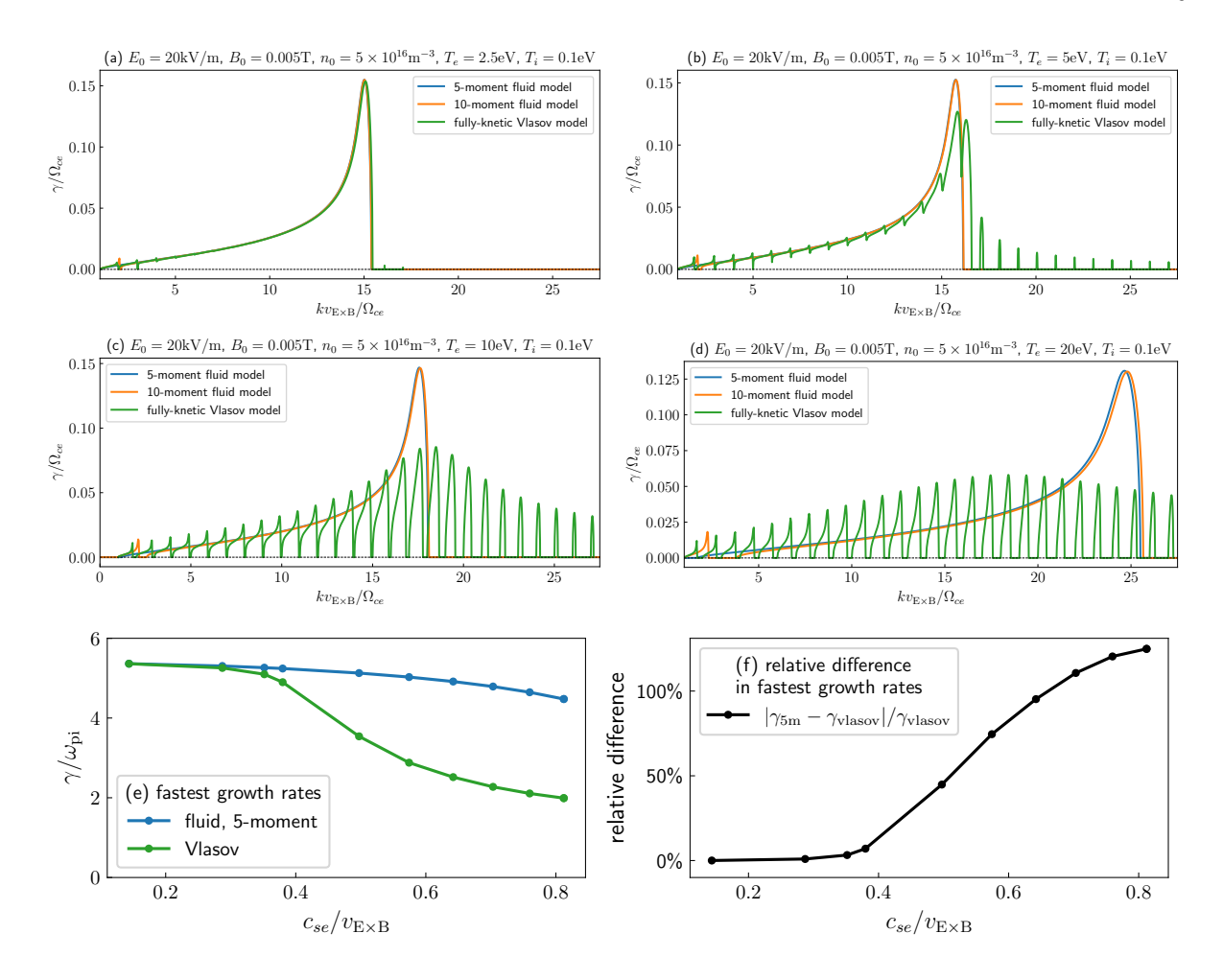


Figure 1. Dispersion relations of the ECDI in fluid moment and fully-kinetic models at different electron/ion temperatures. The parameters are  $E_0 = 20 \text{ kV/m}$ ,  $B_0 = 0.005 \text{ T}$ ,  $n = 5 \times 10^{16} \text{ m}^{-3}$ ,  $T_i = 0.1 \text{ eV}$ , and  $T_e$  values 1 eV, 5 eV, 10 eV, and 20 eV. The 5-moment, 10-moment, and Vlasov dispersion relations are in blue, orange, and green, respectively. Bottom panel (e) shows the growth rates of the fastest-growing mode (FGM) predicted by the 5-moment and the Vlasov models as a function of the ratio  $c_{se}/v_{\rm E\times B}$ . The bottom panel (f) shows the relative error between the 5-moment and Vlasov predictions of the FGM growth rates.

parameters, the relative error is below 25% when the electron sound speed,  $c_{se}$ , is less than about 0.5 times the drift speed  $v_{\text{E}\times\text{B}}$ . Similar estimations hold for typical Hall thruster parameters. At higher temperatures, higher moments would be required for the moment fluid code to achieve good agreement with the fully kinetic model. This will be investigated in future studies. As a first step, this paper will focus on the analysis of the 5-moment model, which will serve as the foundation for future research using higher-moment models.

## C. Location of the fastest-growing mode

In the long wavelength limit, the 5-moment ECDI dispersion relation has two asymptotic solutions: an ion-acoustic-like wave,

$$1 \approx \frac{\omega_{pi}^2}{\omega^2 - k^2 c_{si}^2} \Rightarrow \omega^2 - k^2 c_{si}^2 \approx \omega_{pi}^2, \tag{3}$$

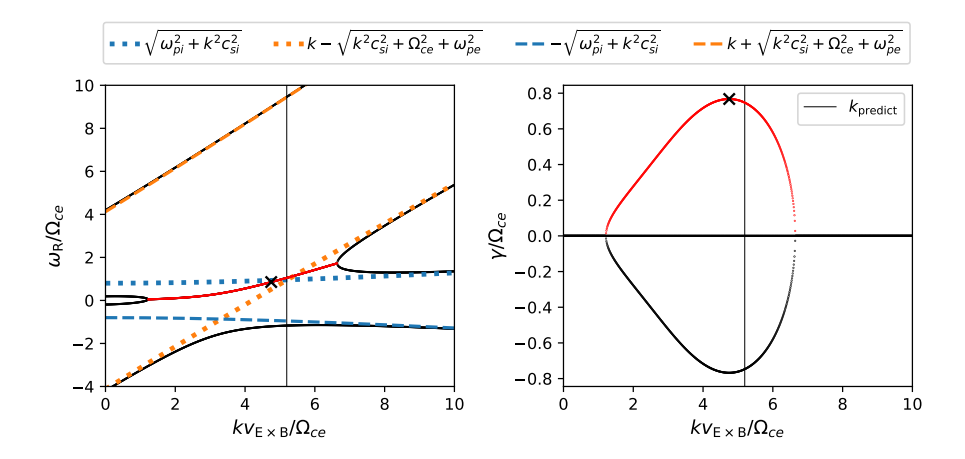


Figure 2. Predicting the location of the fastest-growing mode using the crossing of the ion-acoustic wave (3) and the Doppler-shifted hybrid wave (4). The left and right panels are the k- $\omega$ R and k- $\gamma$  dispersion relation plots, respectively. For better visualization, simplified parameters are employed here:  $m_i/m_e = 25$ ,  $\omega_{pe}/\Omega_{ce} = 4$ ,  $c_{se}/v_{\rm E\times B} = 0.2$ ,  $c_{si}/v_{\rm E\times B} = 0.1$ . The solid curves are the actual dispersion relation: the red curves mark the branch with appreciable growth, while the black curves are the rest of the full dispersion relation. The dotted and dashed lines are asymptotic solutions at the large k limit: the blue lines are the ion-acoustic solution (3), the orange lines are the Doppler-shifted hybrid solution (4). The  $\times$  symbol marks the actual location of the fastest-growing mode in the k > 0,  $\omega > 0$  quadrant. The thin, black vertical lines mark the crossing of the dotted blue and orange asymptotic lines, i.e., the  $k_{\rm FGM}$  given by equation 5 as a prediction of the location of the fastest-growing mode.

and a Doppler-shifted "hybrid" wave, given by

$$1 \approx \frac{\omega_{pe}^2}{\left(\omega - k v_{\text{E} \times \text{B}}\right)^2 - k^2 c_{se}^2 - \Omega_{ce}^2},$$

or

$$(\omega - k v_{\text{E} \times \text{B}})^2 - k^2 c_{se}^2 \approx \Omega_{ce}^2 + \omega_{ne}^2. \tag{4}$$

The unstable region of the 5-moment ECDI on the k- $\omega$  graph is near the crossings of the two waves. Neglecting the  $\omega_{pi}$  terms for simplicity and equating the two asymptotic dispersion relations, we find the wavenumber of the fastest-growing mode (FGM) in the  $\omega > 0$  and k > 0 quadrant,

$$k_{\text{FGM}} \approx \sqrt{\frac{\Omega_{ce}^2 + \omega_{pe}^2}{\left(k v_{\text{E} \times \text{B}} - c_{si}\right)^2 - c_{se}^2}},\tag{5}$$

and the associated real-frequency

$$\omega_{\rm FGM} \approx \sqrt{k_{\rm FGM}^2 c_{si}^2 + \omega_{pi}^2}.$$
 (6)

The agreement between the numerically found (black crosses) and predicted (thin vertical line) locations of the fastest-growing mode is shown in Figure 2 for a set of artificial parameters listed in the figure caption. For a wide range of parameters,  $k_{\text{FGM}}$  and  $\omega_{\text{FGM}}$  give good prediction of the fastest-growing mode's wavenumber and real-frequency, respectively.

## D. Dependence of the fastest growth rate on characteristic parameters

The 5-moment ECDI dispersion relation (2) can be written in the dimensionless form,

$$\frac{1}{r} = \frac{1}{m} \frac{1}{\tilde{\omega}^2 - \tilde{k}^2 c_i^2} + \frac{1}{\left(\tilde{\omega} - \tilde{k}\right)^2 - \tilde{k}^2 c_e^2 - 1},\tag{7}$$

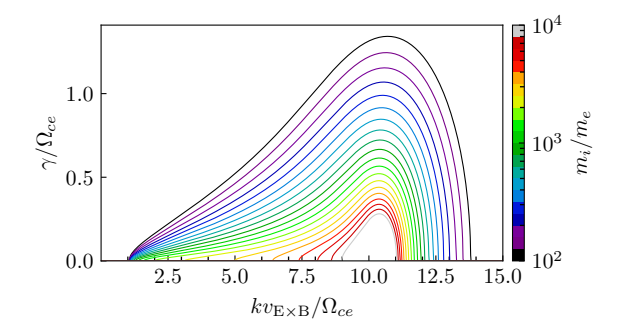


Figure 3. The dependence of the growth rate on the ion-to-electron mass ratio,  $m_i/m_e$ . Different curves represent dispersion relations due to a vast range of  $m_i/m_e$  values. All cases have identical values for the following parameters:  $\omega_{pe}/\Omega_{ce} = 10$ ,  $\sqrt{\gamma p_e/nm_e}/v_{\rm E\times B} = 0.2$ ,  $\sqrt{\gamma p_e/nm_e}/v_{\rm E\times B} = 0.02$ .

where  $\tilde{\omega} \equiv \omega/\Omega_{ce}$ ,  $\tilde{k} \equiv kv_{\rm E\times B}/\Omega_{ce}$ ,  $m \equiv m_i/m_e$ ,  $r = \omega_{pe}/\Omega_{ce}$ ,  $c_e = c_{se}/v_{\rm E\times B}$ ,  $c_i = c_{si}/v_{\rm E\times B}$ . In other words, the 5-moment ECDI dispersion relation is characterized by the four parameters: m, r,  $c_e$ ,  $c_i$ . It is thus useful to further understand how the fastest-growing mode scales with these parameters. To this end, we start from the baseline parameters m = 400,  $c_e = 0.2$ , and  $c_i = 0.02$ , r = 10, and then vary them in isolation to understand how the ECDI mode growth scales. Note that these parameters are chosen not to match experiments but to amplify the effects of each parameter and make the scaling studies below more clear. Note that it is possible to further develop the analytical form of the dispersion relation in various asymptotic limits but those will be left for future work.

Figure 3 shows the dependence of the growth rate on the ion-to-electron mass ratio,  $m_i/m_e$ . It is clear to see that the location of the fastest-growing mode does not change significantly across a vast range of  $m_i/m_e$  ratio. The maximum growth rate, however, drops substantially as the mass ratio increases. The range of unstable wavenumbers also shrinks as the ion-to-electron mass ratio increases, stacking the dispersion relation curves. Another notable observation is that the unstable range has a lower limit at  $k \sim \Omega_{ce}/v_{\rm E\times B}$ . The strong dependence of ECDI on ion-to-electron mass ratio indicates a critical difference in the role of this instability in the space plasmas, dominated by light ions like hydrogen and oxygen, versus HET plasmas, dominated by heavy ions like xenon and sometimes krypton.

Figure 4 demonstrates how the growth rate depends on electron and ion sound speeds, and thus indirectly, the species temperatures. From the left two panels, higher plasma temperature moves the interval with nonzero growth towards greater wavenumbers and small growth rate. A more subtle observation is that the growth rate drops slower with the electron temperature than with the ion temperature. This is evident in the right panel of Figure 4, which shows the maximum growth rate over a matrix of  $c_e$  and  $c_i$  values. In this figure, the gradient along the (vertical) ion axis is much greater than that along the (horizontal) electron axis.

Figure 5 shows the dependence on the  $\omega_{pe}/\Omega_{ce}$  ratio, and thus, indirectly, on the background magnetic field strength. Here, the growth rates (vertical coordinates) are normalized by  $\omega_{pe}$ , which is fixed across all cases. The green curves have comparable  $\omega_{pe}$  and  $\omega_{ce}$ , while the blue curves have  $\Omega_{ce} \gg \omega_{pe}$ , and red curves have  $\Omega_{ce} \ll \omega_{pe}$ . In the strong magnetic field limit (small  $\omega_{pe}/\Omega_{ce}$  and blue curves), the unstable range is very narrow and has large wavenumbers and low growth rates. As the magnetic field weakens and its effect diminishes, the dispersion relation changes less and less as it approaches the Buneman instability in an unmagnetized plasma (the red curves).

## E. Eigenvector and its indication of anomalous electron transport

The matrix-based dispersion relation solver provides the eigenvectors associated with the eigenfrequencies. Here, we consider the parameters  $m \equiv m_i/m_e = 1836$ ,  $r = \omega_{pe}/\Omega_{ce} = 5.07$ ,  $c_e = c_{se}/v_{\rm E\times B} = 0.3$ ,  $c_{si}/v_{\rm E\times B} = 0.0022$ . Its fastest-growing mode occurs at  $k \approx 5.44322\,\Omega_{ce}/v_{\rm E\times B}$  with a growth rate  $\gamma = 0.26892\Omega_{ce}^{-1}$ . Its normalized eigenvector is listed in Table I. Particularly, the value for  $v_{ye1}$  is nontrivial. In linear analysis, this term and the  $v_{xe1}$  perturbation stem from the Lorentz force due to the background magnetic field. A direct consequence of the non-trivial  $v_{ue1}$  value is the development of

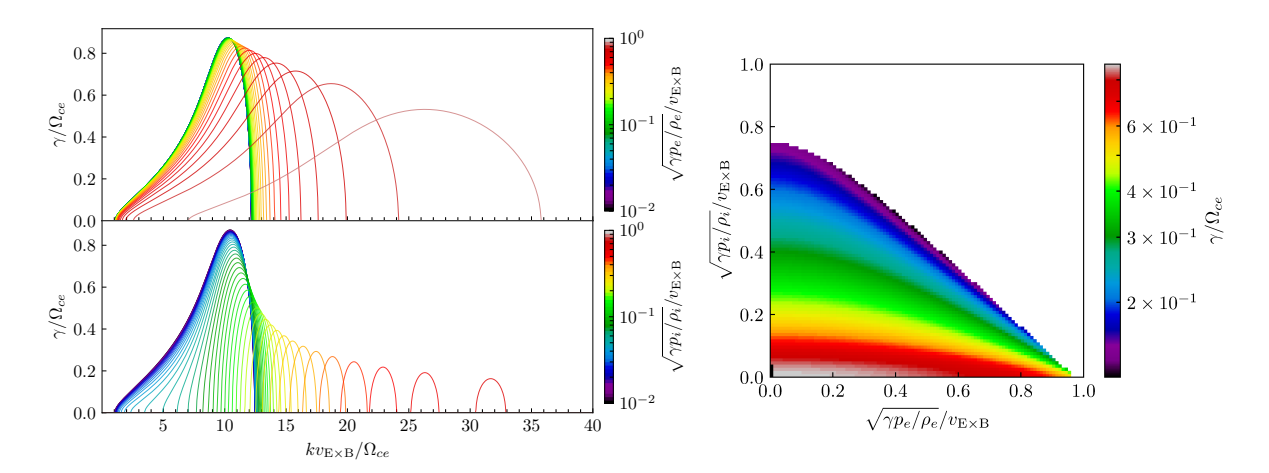


Figure 4. The dependence of the growth rate on the electron and ion sound speeds, and thus indirectly, their temperatures. Left two panels: Different curves represent dispersion relations due to different  $\sqrt{\gamma p_e/nm_e}/v_{\rm E\times B}$  (left top) and  $\sqrt{\gamma p_e/nm_e}/v_{\rm E\times B}$  (left bottom) values. All cases have identical values for  $m_i/m_e=400$  and  $\omega_{pe}/\Omega_{ce}=10$ . Right panel: The fastest-growing-mode growth rates as a function of  $\sqrt{\gamma p_e/nm_e}/v_{\rm E\times B}$  and  $\sqrt{\gamma p_e/nm_e}/v_{\rm E\times B}$ , within the wavenumber interval  $0 < k < 40v_{\rm E\times B}/\Omega_{ce}$ .

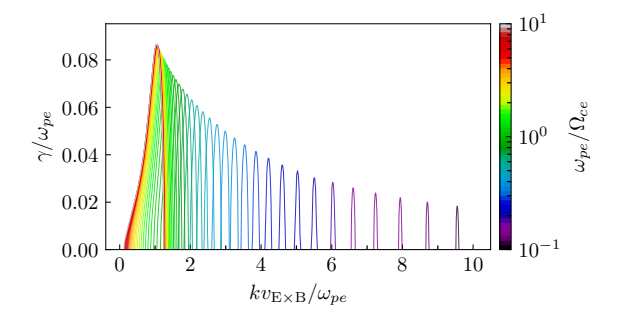


Figure 5. The dependence of the growth rate on the background magnetic field. Different curves represent different  $\omega_{pe}/\Omega_{ce}$  values. All cases have identical values for the following parameters:  $m_i/m_e = 400$ ,  $\sqrt{\gamma p_e/nm_e}/v_{\rm E\times B} = 0.2$ ,  $\sqrt{\gamma p_e/nm_e}/v_{\rm E\times B} = 0.02$ . The growth rates (vertical coordinates) are normalized by  $\omega_{pe}$ .

appreciable anomalous axial (i.e., along the applied electric field) transport of the electrons. Direct numerical simulation of anomalous electron transport is discussed in the next section.

## III. NUMERICAL SIMULATIONS SCANNING SIMPLIFIED PARAMETERS

In this section, we perform direct numerical simulations of the ECDI by integrating the 5-moment equations (1), coupled with the Poisson's equation for the electric field. The simulations are performed using the multi-moment solvers in the Princeton code, Gkeyll [23, 24, 52], that has been verified exten-

$n_{e1}$	$v_{xe1}$	$v_{ye1}$	$v_{ze1}$
0.987	0.0181i	0.0181i	0
$n_{i1}$	$v_{xi1}$	$v_{yi1}$	$v_{zi1}$
0.0636 + 0.109i	-0.000331+0.000666i	0	0

Table I. Normalized eigenvector for the fastest-growing mode for parameters used by the simulation in Section §III.

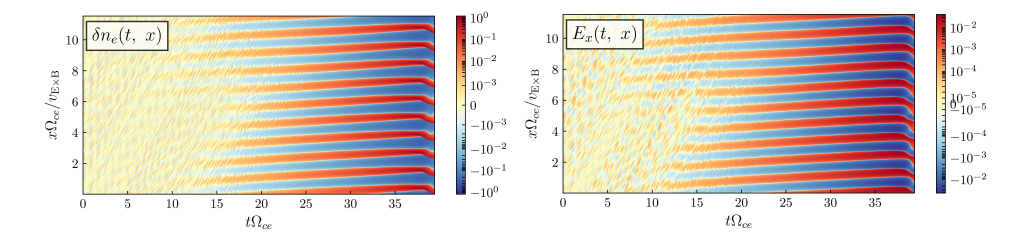


Figure 6. Time evolution of density fluctuation  $\delta n_e \equiv n_e - n_{e0}$  and azimuthal electric field  $E_x$  in the numerical simulation.

sively for a number of plasma physics problems [10, 15, 40–44, 46, 48–50]. Similar models have also been implemented by other groups for various applications [1–3, 29, 32, 35, 36].

## A. Simulation setup

The simulation uses the 1D cross-field configuration, where the simulation domain is along x, the initial electric and magnetic fields are along y and z, so that the initial electron drift is along x. The wavenumber of the fastest-growing mode is  $k_{\rm FGM}=5.44\,\Omega_{ce}/v_{\rm E\times B}$  with a growth rate  $\gamma_{\rm FGM}=0.27\Omega_{ce}^{-1}$ . Its normalized eigenvector is given in II E. The periodic simulation domain length is  $L=10\lambda_{\rm FGM}=10\cdot 2\pi/k_{\rm FGM}=11.54v_{\rm E\times B}/\Omega_{ce}$  and discretized with  $N_x=1280$  cells. The CFL number is 0.95. The gas gamma  $\gamma_{\rm gas}$  is set to 3.

Sinusoidal perturbations are applied to the electrical field  $E_x$  so that the spectral energy  $|E_x(k)|^2$  is evenly distributed across  $kL/2\pi = 0, 1, ..., 32$ . These modes then compete with each other and, over time, the fastest-growing mode, presumably the  $k = k_{\text{FGM}}$  one, dominates. The electron number density  $n_e$  is also perturbed to satisfy Gauss's law initially. Finally, the perturbation magnitudes are controlled by a parameter  $\delta = 10^{-5}$  so that the mode  $E_x(k_m)$  leads to density fluctuation  $\delta \cdot n_e/k_mL$  (and the same  $|E_x(k_m)|$ ).

## B. Linear development

We first examine the development of electron density fluctuation and azimuthal electric field shown in Figure 6. Both show clear dominance of a mode with a wavelength  $\lambda = L/10$ , or  $k = k_{\rm FGM}$  as predicted. Near the end of the simulation at  $t = 40\Omega_{ce}^{-1}$ , the linear development is saturated and the simulation enters a nonlinear stage. In this paper, we focus on the linear stage only.

An interesting observation is that the  $n_e$  and  $E_x$  are not entirely out-of-phase; in other words, a nonzero average  $\langle n_e E_x \rangle$  develops during the simulation. Consistent with Ref. [31], this indicates a nonvanishing cross-field electron mobility in the collisionless limit:  $\mu_{\perp e} = -\langle n_e E_{\rm azimuthal} \rangle / n_e E_{\rm axial} B_{\rm radial}$  and enhances the electron anomalous transport. In the subsequent subsections, we will study the anomalous transport in more detail.

Next, we compare the simulation results with the linear theory prediction. The left panel of Figure 7 shows the snapshots of the electron and ion density fluctuations at the early linear stage, late linear stage, and early nonlinear stage. In the linear stage,  $\delta n_i$  is only a small fraction of  $\delta n_i$ , consistent with the egienvector prediction given in Table. I. Entering the nonlinear stage, the electron density profile becomes highly spiky as the waves start to break. For a more quantitative comparison to theory, the right panel of Figure 7 shows the time evolution of different components of the eigenvectors using electron-to-ion ratios in blue curves, along with their predicted values from the fastest-growing mode as horizontal dashed lines. It is clear that beginning from about  $t=16\Omega_{ce}^{-1}$ , the simulated ratios approaches the predicted values. Again, as predicted by theory, a nonvanishing axial electron transport  $\int v_{ye} dx$  develops and leads to anomalous transport. Near the end of the simulation, where the evolution is nonlinear, the ratios begin to show deviations from the linear prediction. These results provide excellent verification of the linear development in our simulation.

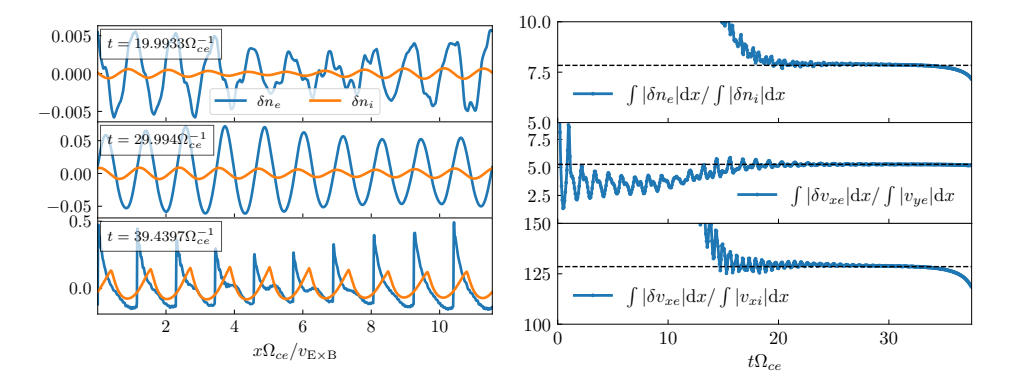


Figure 7. **Left**: Electron and ion number density fluctuation in, from top to bottom, the earlier linear stage, later linear stage, and early nonlinear stage. The competing of various modes, the dominance of the fastest-growing mode, and the steepening of the waves, are evident in these three stages. **Right**: Time evolution of ratios of spatially integrated fluctuations as they approach values from linear-theory predictions of the fastest-growing mode. The integrated quantities, from top to bottom, are  $\int |n_e - n_0| \, dx / \int |n_i - n_0| \, dx$ ,  $\int |v_{xe} - v_{xe0}| \, dx / \int |v_{xi}| \, dx$ , and  $\int |v_{xe} - v_{xe0}| \, dx / \int |v_{ye}| \, dx$ . Their expected values due to the fastest-growing mode from the linear theory are marked by horizontal dashed lines, which are taken from Table I:  $|n_{e1}| / |n_i| \approx 7.8373$ ,  $|v_{xe1}| / |v_{ye1}| \approx 5.27388$ ,  $|v_{xe1}| / |v_{xi1}| \approx 128.562$ .

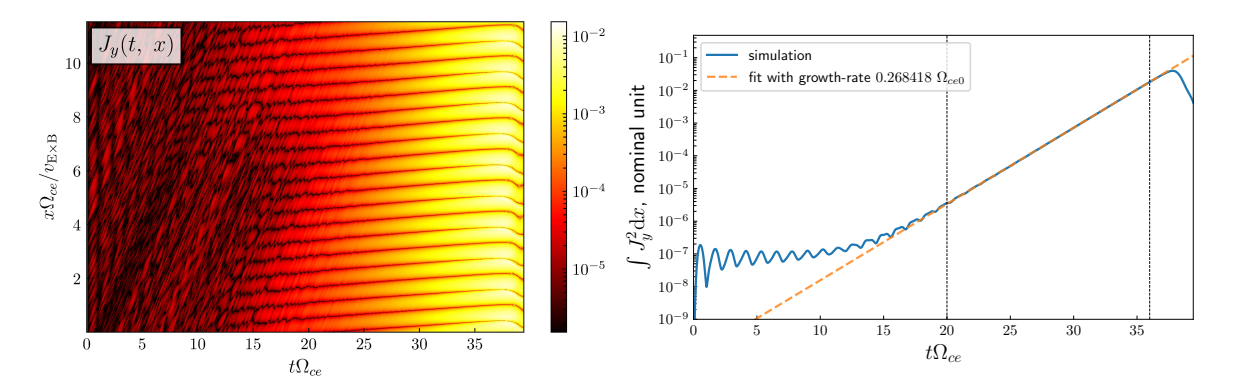


Figure 8. Time evolution of anomalous current in the numerical simulation. Left: Anomalous axial current  $J_y$  as a function of (t, x). The horizontal and vertical axes are time and x-coordinates, respectively. Note that in this simulation  $J_y$  is due to the anomalous transport of electrons only since ions are unmagnetized and do not contribute to  $J_y$ . Right: Time evolution of the anomalous current,  $\int_0^L J_y dx$ , integrated over the entire domain (blue curve) along with a linear fit (orange dashed line). The vertical dashed lines mark the range where the fit is made.

## C. Anomalous electron transport

As mentioned earlier, the correlated fluctuations in  $n_e$  and  $E_x$  indicate the existence of anomalous electron transport. The left panel of Figure 8 shows the temporal-spatial profile of the anomalous electron current. A positive net current develops in the linear stage at the predicted wavelength. The right panel shows the growth of the integrated anomalous current. In the early stage of the simulation, the competition between modes of different wavelengths causes a wide spectrum of fluctuations. Beginning from about  $t=16\Omega_{ce}^{-1}$ , one dominant mode arises and its linear growth lasts about  $20\Omega_{ce}^{-1}$ , which is determined by the initial perturbation level. Fitting the data between the primary region of linear growth, at approximately  $20 < t\Omega_{ce} < 37.5$ , we find a growth rate  $\gamma = 0.268418\Omega_{ce}$ , which is in excellent agreement with the theoretical prediction  $0.26892\Omega_{ce}$ .

So far, we have shown the development of nonzero  $\langle n_e E_x \rangle$  and the electron anomalous current. It is useful to further examine how they are related. We start by examining the electron momentum equation

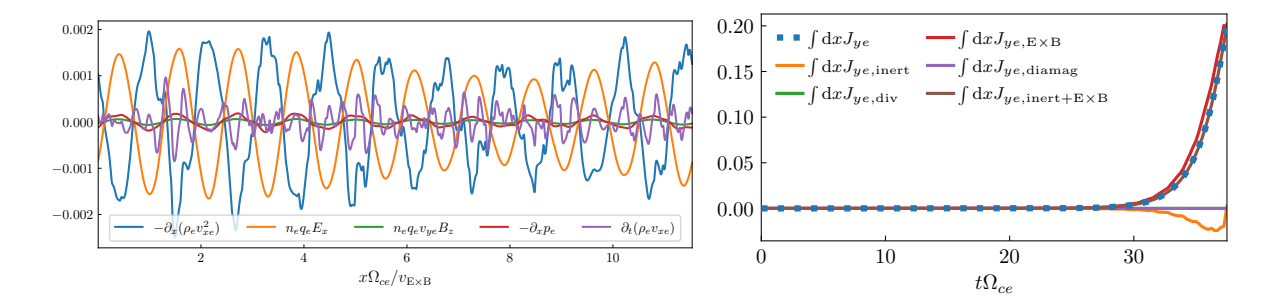


Figure 9. Left: Components of the electron momentum equation along the x (azimuthal) direction in the midlinear stage at  $t=25\Omega_{ce}^{-1}$ . The magenta term (the last term in the figure legend) is the net acceleration and are the summation of the remaining terms. Right: Temporal development of the spatially-integrated axial electron current  $\int_0^L J_{ye} dx$  (dotted blue curve) and its decomposition (various solid curves). The terms corresponding equation (9) are  $J_{ye} = n_e q_e v_{ey}$ ,  $J_{ye,\text{E}\times\text{B}} = n_e q_e E_x/B_z$ ,  $J_{ye,\text{inert}} = -\partial_t \left(\rho_e v_{xe}\right)/B_z$ ,  $J_{ye,\text{diamag}} = -\partial_x p_e/B_z$ .

along the azimuthal direction x,

$$\frac{\partial (\rho_e v_{xe})}{\partial t} + \frac{\partial p_e}{\partial x} + \frac{\partial (\rho_e v_{xe}^2)}{\partial x} 
= n_e q_e (E_x + v_{ey} B_z),$$
(8)

to understand the role of the azimuthal electric force term  $n_e q_e E_x$ . The left panel of Figure 9 shows the decomposition of this equation in the middle of the linear stage at  $t=25\Omega_{ce}^{-1}$ . In this snapshot, The pressure gradient force (red) is smaller in magnitude and the  $V\times B$  force (green) term is negligible. The  $n_e q_e E_x$  term (orange) and the flow divergence term  $\partial_x \left(\rho v_{xe}^2\right)$  (blue) are much larger in magnitude but appear to largely cancel each other. The net acceleration, i.e., the time derivative term (magenta), is a fraction of the  $n_e q_e E_x$  and  $\partial_x \left(\rho v_{xe}^2\right)$  terms, indicating the importance of both terms.

Next, we divide this momentum equation by  $B_z$  and integrate each of the components of Eq. 8 along the x-coordinate at every time step. This way, we obtain the time evolution of the net and decomposed currents along the y-direction (axial),

$$\int dx \left[ n_e q_e v_{ey} + \frac{n_e q_e E_x}{B_z} - \frac{1}{B_z} \frac{\partial (\rho_e v_{xe})}{\partial t} - \frac{1}{B_z} \frac{\partial p_e}{\partial x} - \frac{1}{B_z} \frac{\partial (\rho_e v_{xe}^2)}{\partial x} \right]. \tag{9}$$

The results are shown in the right panel of Figure 9. Here, the dashed curve is the total current  $\int n_e q_e v_{ye} dx$ . The current due to the flow divergence term (green) and the pressure gradient (magenta) are negligible. The main contribution comes from the  $E_x \times B_z$  current  $\int dx n_e q_e E_x/B_z$  (red), with small cancellation due to time-derivative inertial term,  $-\int dx \partial_t \left(\rho_e v_{xe}\right)/B_z$  (orange). The sum of the two agrees with the net anomalous current very well. Therefore, in this simulation, the anomalous electron current is supported by the  $E \times B$  flux, consistent with some previous works [31] but differs from the conclusions of [27] (the latter observed  $E \times B$  fluxes that is not large enough to fully account for the anomalous transport). A more comprehensive understanding of this issue would require exhaustive numerical experiments in various parameter regimes and could be the topic of future work.

## IV. 5-MOMENT FLUID VS. FULLY-KINETIC SIMULATIONS USING EXPERIMENTAL PARAMETERS

In this section, we compare 1D 5-moment and fully-kinetic Vlasov-Poisson simulations of the instability using parameters relevant to E × B devices. The goal is to demonstrate the capability and limitations of the model for realistic, experimental parameters, particularly in the linear growth and saturation of the anomalous electron current. We chose the second case in the linear theory comparison in Section IIB which has  $E_0 = 20 \text{ kV/m}$ ,  $B_0 = 0.005 \text{ T}$ ,  $m_i/m_e = 241074$ ,  $n_0 = 5 \times 10^{16} \text{ m}^3$ ,  $T_e = 5 \text{ eV}$ , and

 $T_i = 0.1$  eV. These parameters give the dispersion relations shown in Figure 1b, or the zoomed-in version of Figure 10a.

The simulation coordinates are consistent with those used in Section III. The domain length is set to  $L_x=4\,\mathrm{cm}$  and 30 modes in the electron density were initialized at wavenumbers  $k_m=2\pi m/L_x$ ,  $m=1,2,\cdots 30$ , with relative density fluctuations  $\delta n_m/n_0=m\times 10^{-7}$  so that all modes have equal magnitudes of electric field fluctuations. These wavenumbers are marked by vertical dashed lines in Figure 10a. Particularly, the orange, green, and red vertical lines denote mode numbers m=21, 22, and 23, which are within the range of peak growths. In these initialized modes, the 5-moment prediction's  $m=22\,\mathrm{mode}$  has the greatest growth rate  $\gamma\approx 0.152\,\Omega_{ce0}$ , and the  $m=21\,\mathrm{mode}$  has the second greatest  $\gamma\approx 0.091\,\Omega_{ce0}$ . The kinetic prediction's m=21, 22, and 23 modes have growth rates  $\gamma\approx 0.0691\,\Omega_{ce0}$ ,  $\gamma\approx 0.120\,\Omega_{ce0}$ , and  $0.107\,\Omega_{ce0}$ , respectively.

For the kinetic simulation, we used the continuum Vlasov-Poisson module available in Gkeyll v2 (the same code providing the 5-moment fluid simulation)[9, 30]. The kinetic simulation uses a Discontinuous-Galerkin finite-element scheme and 2nd-order Serendipity bases for spatial discretization and a 2nd-order Strong-Stability preserving Runge-Kutta (SSP-RK2) scheme for time integration. The number of spatial cells are 2560 and 320, respectively, in the 5-moment and Vlasov simulations. The kinetic simulation also uses a square  $v_x \times v_y$  velocity domain of widths  $24\,v_{\rm ths}$  and cell numbers 64 for either species s=e,i.

Figure 10b shows the growth of total spatially integrated anomalous electron current power in the two simulations. Fitting of the 5-moment simulation between  $40 < t\Omega_{ce0} < 90$  gives a linear growth rate  $\gamma \approx 0.15\,\Omega_{ce0}$ , in excellent agreement with the theoretical prediction. Fitting of the kinetic simulation gives a growth rate  $\gamma \approx 0.11\,\Omega_{ce0}$ , between the first two fastest growth rates predicted, as they are close in the first place. It is interesting to note that two simulations come down to comparable plateau values. Therefore, for these parameters, the 5-moment simulation gives a qualitatively reasonable prediction of the saturation level for the total anomalous current in terms of order of magnitude. The agreement would vary with the parameters like the electron temperature.

As implied by the dispersion relations in Figure 10a, the kinetic simulation would allow two comparable modes to develop at m=22 and 23, while the 5-moment fluid simulation only has one dominating mode at m=22. The simulations confirmed this difference. Figure 10c shows the power of different Fourier components of the anomalous current  $J_{ye}$  (for simplicity, only the dominating modes between  $21 \le m \le 23$  are shown). The simulations clearly captured the expected linear growth rates, marked by thick, translucent straight lines, for either model.

Figure 11 shows the configuration and wavenumber space profiles of the anomalous current during typical linear (left, at  $t=80\,\Omega_{ce0}^{-1}$ ) and saturation (left, at  $t=160\,\Omega_{ce0}^{-1}$ ) stages. In the linear stage, both the spatial profile and Fourier component powers clearly show the dominance of the m=22 mode in the 5-moment simulation, while the kinetic simulation shows the overlapping of and competence between the m=22 and m=23 modes. In the saturation stage, the 5-moment simulation patterns become very "spiky" and remain dominated by the single m=22 mode, while the kinetic simulation develops a broader range of wave modes, notably at larger wavelengths.

In summary, using realistic experimental parameters and at relatively low electron temperature, the 5-moment fluid model is capable of capturing the growth of anomalous current roughly in the correct regime. The 5-moment model itself clearly lacks the broad electron harmonics excited in the fully-kinetic simulation, but the total saturated anomalous current seems to be a good indicator of the kinetic values for lower temperatures. Again, such agreement relies on the parameter regime and becomes less satisfactory as the temperature rises and higher cyclotron harmonics become important. On the other hand, the multifluid high-moment model may indeedcapture more cyclotron harmonics by including higher velocity moments in future studies.

## V. DISCUSSIONS AND CONCLUSIONS

The ECDI due to the electron  $E \times B$  drift in a cross-field setup is an important research topic actively studied in the HET community and has been drawing increased attention from the space physics community as well. Traditional ECDI studies often rely on fully kinetic models. Models based on the fluid or hybrid description are often thought to require additional collision models and adjustable parameters to correctly capture produce anomalous transport. In this paper, we show detailed theoretical proof and numerical evidence how this instability develops in a collisionless two-fluid plasma, and leads to

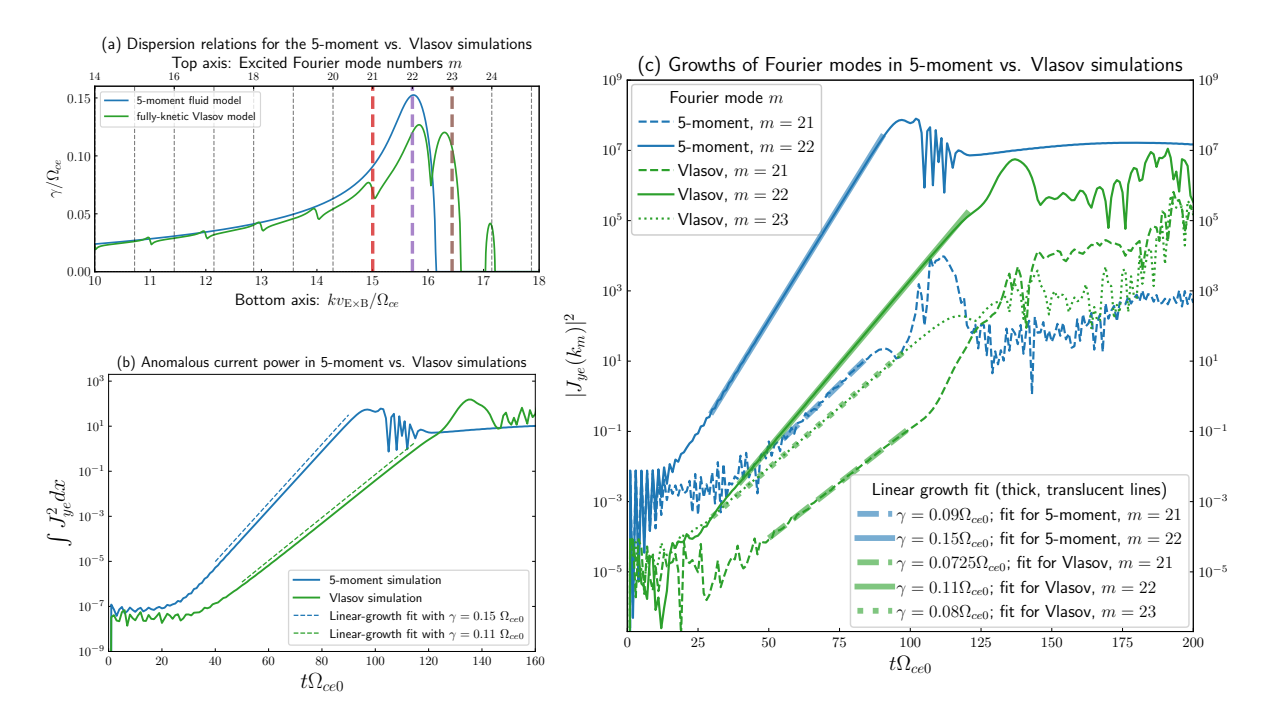


Figure 10. Comparison of 5-moment and Vlasov simulations in Section. IV using parameters  $E_0 = 20 \text{ kV/m}$ ,  $B_0 = 0.005 \text{ T}$ ,  $m_i/m_e = 241074$ ,  $n_0 = 5 \times 10^{16} \text{ m}^3$ ,  $T_e = 5 \text{ eV}$ , and  $T_i = 0.1 \text{ eV}$ . All 5-moment diagnostics are in blue, and all Vlasov diagnostics are in green. **Upper left panel (a)**: Dispersion relations of the ECDI for parameters used in the comparative 5-moment vs. Vlasov simulations. This panel is a zoomed-in version of Figure 1b with additional vertical dashed lines marking wavenumbers of initial Fourier modes  $k_m = 2\pi m/L_x$ , where mode numbers  $m = 1, 2, \dots, 30$ . Particularly, the red, purple, and brown vertical lines denote mode numbers m = 21, 22, and 23, which are within the range of peak growths for either model. **Lower left panel (b)**: Time evoluation of the integrated electron anomalous current power in the 5-moment (blue curve) and Vlasov (green curve) simulations. The dashed straight lines represent the linear-growth fits for the two runs. **Right panel (c)**: The growth of different Fourier modes in the 5-moment (blue curves) and Vlasov (green curves) simulations, and linear-growth fits (thick, translucent straight lines).

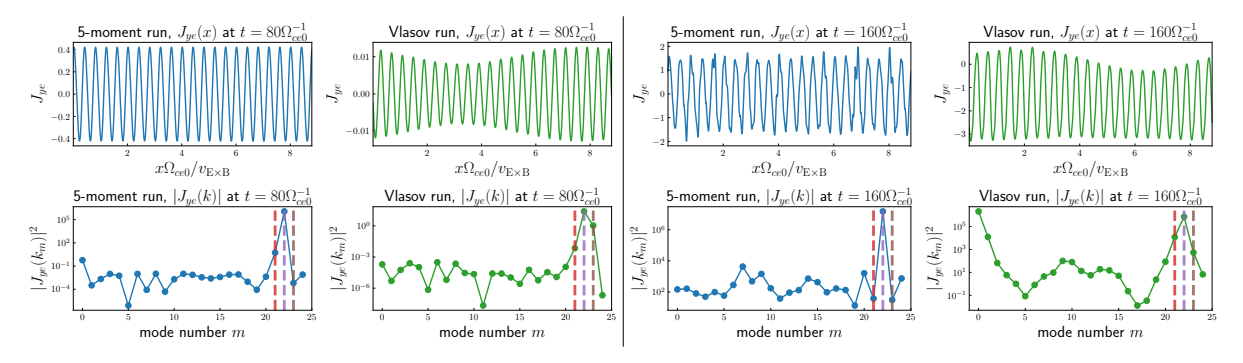


Figure 11. More comparison of 5-moment and Vlasov simulations in Section. IV. Left four panels: For a linear stage frame at  $t=80\,\Omega_{ce0}^{-1}$ , the spatial profile of the anomalous current in the 5-moment (upper left, blue line) and Vlasov (upper right, green line) simulations, the power of the first Fourier modes (lower left, blue line with dots) and Vlasov (lower right, green line with dots) simulations. Consistent with Figure 10a, the red, purple, and brown vertical dashed lines denote mode numbers  $m=21,\,22,\,$  and 23. Right four panels: The same diagnostics in the saturation stage at  $t=160\,\Omega_{ce0}^{-1}$ .

enhanced axial electron anomalous transport.

In the 5-moment model, only the lowest-order electron resonance is captured, and the coupling between a Doppler shifted hybrid wave associated with this resonance, and an ion-acoustic-like wave, leads to the development of ECDI. Compared to the fully kinetic theory featured by a highly quantized nature of the unstable modes due to higher-order electron resonances, the 5-moment gives reasonable prediction of the fastest-growing mode in terms of both wavelength and growth rate, when the plasma temperature is low. The prediction gets worse in comparison to fully kinetic descriptions as the plasma temperature increases.

As indicated by the secondary unstable branch when using the 10-moment model, we may capture a more accurate dispersion relation, including the discrete patterns noted in the kinetic description, by including higher fluid moments. Due to the very low cost of these fluid moment models, this provides a promising new approach for future modeling of HETs and other space physics phenomena where cross-field instabilities are important.

We presented preliminary comparison against fully-kinetic simulations using realistic, experimental parameters, which confirmed the model's ability to predict the growth and saturation of anomalous current roughly in the correct regime at relatively low electron temperatures. The comparison also shows the model's inherent limitation of not being able to excite higher harmonics and broader wave modes, which may be partially overcome by including higher velocity moments (like the heat-flux tensor) in the fluid equations. Finally, it should be noted that, the focus of this work is on the fundamental properties and scaling of the dispersion relation and the development of anomalous transport without additional collisions. The work performed here may be extended in the future to use the 10-moment model, and possibly even higher-order moment fluid models, with improved plasma closure relations based on physical constraints [2, 4, 5, 25, 42, 44] or data-driven approaches [12].

## ACKNOWLEDGMENTS

This work was supported by the Air Force Office of Scientific Research under grant number FA9550-15-1-0193. The work of Bhuvana Srinivasan was supported by the National Science Foundation under grant number PHY-1847905. The work of Ammar Hakim was also partially supported via DOE contract DE-AC02-09CH11466 for the Princeton Plasma Physics Laboratory. Liang Wang thanks Manaure Francisquez for suggestions on continuum Vlasov-Poisson simulations.

<sup>[1]</sup> Remi Abgrall and Harish Kumar. Robust Finite Volume Schemes for Two-Fluid Plasma Equations. *J. Sci. Comput.*, 60(3):584–611, sep 2014. ISSN 0885-7474.

<sup>[2]</sup> F. Allmann-Rahn, T. Trost, and R. Grauer. Temperature gradient driven heat flux closure in fluid simulations of collisionless reconnection. *Journal of Plasma Physics*, 84(3), June 2018. doi:10.1017/s002237781800048x. URL https://doi.org/10.1017/s002237781800048x.

<sup>[3]</sup> F Allmann-Rahn, S Lautenbach, R Grauer, and RD Sydora. Fluid simulations of three-dimensional reconnection that capture the lower-hybrid drift instability. *Journal of Plasma Physics*, 87(1), 2021.

<sup>[4]</sup> S. Boccelli, J. G. McDonald, and T. E. Magin. 14-moment maximum-entropy modeling of collisionless ions for hall thruster discharges. *Physics of Plasmas*, 29(8):083903, 2022. doi:10.1063/5.0100092. URL https://doi.org/10.1063/5.0100092.

<sup>[5]</sup> Stefano Boccelli, Thomas Charoy, Alejandro Alvarez Laguna, Pascal Chabert, Anne Bourdon, and Thierry E Magin. Collisionless ion modeling in hall thrusters: Analytical axial velocity distribution function and heat flux closures. *Physics of Plasmas*, 27(7):073506, 2020.

<sup>[6]</sup> Jean Pierre Boeuf. Tutorial: Physics and modeling of Hall thrusters. J. Appl. Phys., 121(1), 2017. ISSN 10897550.

<sup>[7]</sup> A. W. Breneman, C. A. Cattell, K. Kersten, A. Paradise, S. Schreiner, P. J. Kellogg, K. Goetz, and L. B. Wilson. STEREO and Wind observations of intense cyclotron harmonic waves at the Earth's bow shock and inside the magnetosheath. J. Geophys. Res. Sp. Phys., 118(12):7654-7664, 2013. ISSN 21699402.

<sup>[8]</sup> O Buneman. Instability of electrons drifting through ions across a magnetic field. Journal of Nuclear Energy. Part C, Plasma Physics, Accelerators, Thermonuclear Research, 4(2):111-117, January 1962. doi: 10.1088/0368-3281/4/2/305. URL https://doi.org/10.1088/0368-3281/4/2/305.

- [9] P. Cagas, A. Hakim, J. Juno, and B. Srinivasan. Continuum kinetic and multi-fluid simulations of classical sheaths. *Phys. Plasmas*, 24(2):022118, feb 2017. ISSN 1070-664X.
- [10] Petr Cagas, Ammar Hakim, Wayne Scales, and Bhuvana Srinivasan. Nonlinear saturation of the weibel instability. Physics of Plasmas, 24(11):112116, 2017.
- [11] L. J. Chen, S. Wang, L. B. Wilson, S. Schwartz, N. Bessho, T. Moore, D. Gershman, B. Giles, D. Malaspina, F. D. Wilder, R. E. Ergun, M. Hesse, H. Lai, C. Russell, R. Strangeway, R. B. Torbert, F. A. Vinas, J. Burch, S. Lee, C. Pollock, J. Dorelli, W. Paterson, N. Ahmadi, K. Goodrich, B. Lavraud, O. Le Contel, Yu V. Khotyaintsev, P. A. Lindqvist, S. Boardsen, H. Wei, A. Le, and L. Avanov. Electron Bulk Acceleration and Thermalization at Earth's Quasiperpendicular Bow Shock. *Phys. Rev. Lett.*, 120(22):225101, 2018. ISSN 10797114.
- [12] Wenjie Cheng, Haiyang Fu, Liang Wang, Chuanfei Dong, Yaqiu Jin, Mingle Jiang, Jiayu Ma, Yilan Qin, and Kexin Liu. Data-driven, multi-moment fluid modeling of landau damping. Computer Physics Communications, page 108538, 2022. ISSN 0010-4655. doi:https://doi.org/10.1016/j.cpc.2022.108538. URL https://www.sciencedirect.com/science/article/pii/S0010465522002570.
- [13] EY Choueiri. Plasma oscillations in hall thrusters. Physics of Plasmas, 8(4):1411-1426, 2001.
- [14] Z. A. Cohen, C. A. Cattell, A. W. Breneman, L. Davis, P. Grul, K. Kersten, L. B. Wilson III, and J. R. Wygant. The rapid variability of wave electric fields within and near quasiperpendicular interplanetary shock ramps: STEREO observations. *The Astrophysical Journal*, 904(2):174, December 2020. doi:10.3847/1538-4357/abbeec. URL https://doi.org/10.3847/1538-4357/abbeec.
- [15] Chuanfei Dong, Liang Wang, Ammar Hakim, Amitava Bhattacharjee, James A. Slavin, Gina A. Dibraccio, Kai Germaschewski, Amitava Bhattacharjee, James A. Slavin, Gina A. Dibraccio, and Kai Germaschewski. Global Ten-Moment Multifluid Simulations of the Solar Wind Interaction with Mercury: From the Planetary Conducting Core to the Dynamic Magnetosphere. Geophys. Res. Lett., page 2019GL083180, nov 2019. ISSN 0094-8276.
- [16] D. Forslund, R. Morse, C. Nielson, and J. Fu. Electron cyclotron drift instability and turbulence. Phys. Fluids, 15(7):1303–1318, 1972. ISSN 10706631.
- [17] D. W. Forslund, R. L. Morse, and C. W. Nielson. Electron Cyclotron Drift Instability. Phys. Rev. Lett., 25 (18):1266–1270, nov 1970. ISSN 0031-9007.
- [18] D. W. Forslund, R. L. Morse, and C. W. Nielson. Nonlinear Electron-Cyclotron Drift Instability and Turbulence. Phys. Rev. Lett., 27(21):1424–1428, nov 1971. ISSN 0031-9007.
- [19] S. Peter Gary. Longitudinal waves in a perpendicular collisionless plasma shock: II. Vlasov ions. *J. Plasma Phys.*, 4(4):753–760, dec 1970. ISSN 0022-3778.
- [20] S. Peter Gary and J. J. Sanderson. Longitudinal waves in a perpendicular collisionless plasma shock: I. Cold ions. J. Plasma Phys., 4(4):739–751, dec 1970. ISSN 0022-3778.
- [21] Dan M Goebel and Ira Katz. Fundamentals of electric propulsion: Ion and hall thrusters. John Wiley & Sons, Nashville, TN, 2008.
- [22] Katherine A. Goodrich, Robert Ergun, Steven J. Schwartz, Lynn B. Wilson, David Newman, Frederick D. Wilder, Justin Holmes, Andreas Johlander, James Burch, Roy Torbert, Yuri Khotyaintsev, Per Arne Lindqvist, Robert Strangeway, Christopher Russell, Daniel Gershman, Barbara Giles, and Laila Andersson. MMS Observations of Electrostatic Waves in an Oblique Shock Crossing. J. Geophys. Res. Sp. Phys., 123 (11):9430-9442, 2018. ISSN 21699402.
- [23] A. Hakim, J. Loverich, and U. Shumlak. A high resolution wave propagation scheme for ideal Two-Fluid plasma equations. J. Comput. Phys., 219:418–442, 2006. ISSN 00219991.
- [24] Ammar H. Hakim. Extended MHD modeling with the ten-moment equations. J. Fusion Energy, 27:36–43, 2008. ISSN 01640313.
- [25] Gregory W. Hammett and Francis W. Perkins. Fluid moment models for Landau damping with application to the ion-temperature-gradient instability. *Phys. Rev. Lett.*, 64(25):3019–3022, jun 1990. ISSN 0031-9007.
- [26] Kentaro Hara. An overview of discharge plasma modeling for Hall effect thrusters. Plasma Sources Sci. Technol., 28(4), 2019. ISSN 13616595.
- [27] Salomon Janhunen, Andrei Smolyakov, Oleksandr Chapurin, Dmytro Sydorenko, Igor Kaganovich, and Yevgeni Raitses. Nonlinear structures and anomalous transport in partially magnetized ExB plasmas. *Phys. Plasmas*, 25(1), 2018. ISSN 10897674.
- [28] Salomon Janhunen, Andrei Smolyakov, Dmytro Sydorenko, Marilyn Jimenez, Igor Kaganovich, and Yevgeny Raitses. Evolution of the electron cyclotron drift instability in two-dimensions. *Phys. Plasmas*, 25(8), 2018. ISSN 10897674.
- [29] Valentin Joncquieres, François Pechereau, Alejandro Alvarez Laguna, Anne Bourdon, Olivier Vermorel, and Benedicte Cuenot. A 10-moment fluid numerical solver of plasma with sheaths in a hall effect thruster. In 2018 Joint Propulsion Conference, page 4905, 2018.
- [30] J. Juno, A. Hakim, J. TenBarge, E. Shi, and W. Dorland. Discontinuous galerkin algorithms for fully kinetic plasmas. *Journal of Computational Physics*, 353:110–147, January 2018. doi:10.1016/j.jcp.2017.10.009. URL https://doi.org/10.1016/j.jcp.2017.10.009.

- [31] T. Lafleur, S. D. Baalrud, and P. Chabert. Theory for the anomalous electron transport in Hall effect thrusters. I. Insights from particle-in-cell simulations. *Phys. Plasmas*, 23(5), 2016. ISSN 10897674.
- [32] Alejandro Alvarez Laguna, Teddy Pichard, Thierry Magin, Pascal Chabert, Anne Bourdon, and Marc Massot. An asymptotic preserving well-balanced scheme for the isothermal fluid equations in low-temperature plasma applications. 2019.
- [33] M. Lampe, W. M. Manheimer, J. B. McBride, J. H. Orens, R. Shanny, and R. N. Sudan. Nonlinear Development of the Beam-Cyclotron Instability. *Phys. Rev. Lett.*, 26(20):1221–1225, may 1971. ISSN 0031-9007.
- [34] M. Lampe, W. M. Manheimer, J. B. McBride, J. H. Orens, K. Papadopoulos, R. Shanny, and R. N. Sudan. Theory and simulation of the beam cyclotron instability. *Phys. Fluids*, 15(4):662–675, 1972. ISSN 10706631.
- [35] ET Meier and U Shumlak. Development of five-moment two-fluid modeling for z-pinch physics. Physics of Plasmas, 28(9):092512, 2021.
- [36] S. T. Miller and U. Shumlak. A multi-species 13-moment model for moderately collisional plasmas. Phys. Plasmas, 23(8):082303, aug 2016. ISSN 1070-664X.
- [37] L. Muschietti and B. Lembège. Electron cyclotron microinstability in the foot of a perpendicular shock: A self-consistent PIC simulation. Adv. Sp. Res., 37(3):483–493, jan 2006. ISSN 02731177.
- [38] L. Muschietti and B. Lembège. Microturbulence in the electron cyclotron frequency range at perpendicular supercritical shocks. J. Geophys. Res. Sp. Phys., 118(5):2267–2285, may 2013. ISSN 21699380.
- [39] Laurent Muschietti and Bertrand Lembège. Two-stream instabilities from the lower-hybrid frequency to the electron cyclotron frequency: application to the front of quasi-perpendicular shocks. *Ann. Geophys.*, 35(5): 1093–1112, sep 2017. ISSN 1432-0576.
- [40] Jonathan Ng, Yi-Min Huang, Ammar Hakim, Amitava Bhattacharjee, Adam Stanier, William Daughton, Liang Wang, and Kai Germaschewski. The island coalescence problem: Scaling of reconnection in extended fluid models including higher-order moments. *Phys. Plasmas*, 22(11):112104, nov 2015. ISSN 1070-664X.
- [41] Jonathan Ng, Ammar Hakim, A. Bhattacharjee, Adam Stanier, and W. Daughton. Simulations of antiparallel reconnection using a nonlocal heat flux closure. *Phys. Plasmas*, 24(8):082112, aug 2017. ISSN 1070-664X.
- [42] Jonathan Ng, Ammar Hakim, and A. Bhattacharjee. Using the maximum entropy distribution to describe electrons in reconnecting current sheets. *Phys. Plasmas*, 25(8):082113, aug 2018. ISSN 1070-664X.
- [43] Jonathan Ng, Ammar Hakim, James Juno, and Amitava Bhattacharjee. Drift Instabilities in Thin Current Sheets Using a Two-Fluid Model With Pressure Tensor Effects. J. Geophys. Res. Sp. Phys., 124(5):3331– 3346, may 2019. ISSN 2169-9380.
- [44] Jonathan Ng, A. Hakim, L. Wang, and A. Bhattacharjee. An improved ten-moment closure for reconnection and instabilities. *Physics of Plasmas*, 27(8):082106, August 2020.
- [45] A I Smolyakov, O Chapurin, W Frias, O Koshkarov, I Romadanov, T Tang, M Umansky, Y Raitses, I D Kaganovich, and V P Lakhin. Fluid theory and simulations of instabilities, turbulent transport and coherent structures in partially-magnetized plasmas of \$\mathbf{e}\\times \mathbf{b}\$\$ discharges. Plasma Physics and Controlled Fusion, 59(1):014041, November 2016. doi:10.1088/0741-3335/59/1/014041. URL https://doi.org/10.1088/0741-3335/59/1/014041.
- [46] Bhuvana Srinivasan and Ammar Hakim. Role of electron inertia and electron/ion finite larmor radius effects in low-beta, magneto-rayleigh-taylor instability. *Physics of Plasmas*, 25(9):092108, 2018.
- [47] F. Taccogna and L. Garrigues. Latest progress in hall thrusters plasma modelling. Reviews of Modern Plasma Physics, 3(1), July 2019. doi:10.1007/s41614-019-0033-1. URL https://doi.org/10.1007/s41614-019-0033-1.
- [48] Jason M. TenBarge, J. Ng, James Juno, Liang Wang, Ammar H. Hakim, A. Bhattacharjee, Ng Jonathan, James Juno, Liang Wang, Ammar H. Hakim, and Amitava Battacharjee. An Extended MHD Study of the 16 October 2015 MMS Diffusion Region Crossing. J. Geophys. Res. Sp. Phys., pages 1–14, 2019. ISSN 21699402.
- [49] Liang Wang, Ammar H. A.H. Hakim, A. Bhattacharjee, and K. Germaschewski. Comparison of multi-fluid moment models with particle-in-cell simulations of collisionless magnetic reconnection. *Phys. Plasmas*, 22 (1):012108, jan 2015. ISSN 1070-664X.
- [50] Liang Wang, Kai Germaschewski, Ammar Hakim, Chuanfei Dong, Joachim Raeder, and Amitava Bhattacharjee. Electron Physics in 3-D Two-Fluid 10-Moment Modeling of Ganymede's Magnetosphere. J. Geophys. Res. Sp. Phys., 123(4):2815–2830, apr 2018. ISSN 21699402.
- [51] Liang Wang, Ammar Hakim, and Bhuvana Srinivasan. XENON: A matriX-based dispErsioN relatiON solver for plasma physics, 2019. URL https://github.com/liangwang0734/xenon.
- [52] Liang Wang, Ammar H. Hakim, Jonathan Ng, Chuanfei Dong, and Kai Germaschewski. Exact and locally implicit source term solvers for multifluid-Maxwell systems. J. Comput. Phys., 2020. ISSN 10902716.
- [53] L. B. Wilson, C. A. Cattell, P. J. Kellogg, K. Goetz, K. Kersten, J. C. Kasper, A. Szabo, and M. Wilber. Large-amplitude electrostatic waves observed at a supercritical interplanetary shock. J. Geophys. Res. Sp. Phys., 115(12):1–14, 2010. ISSN 21699402.

- [54] L. B. Wilson, D. G. Sibeck, A. W. Breneman, O. Le Contel, C. Cully, D. L. Turner, V. Angelopoulos, and D. M. Malaspina. Quantified energy dissipation rates in the terrestrial bow shock: 2. Waves and dissipation. J. Geophys. Res. Sp. Phys., 119(8):6475–6495, 2014.
- [55] H. V. Wong. Electrostatic electron-ion streaming instability. Phys. Fluids, 13(3):757–760, 1970. ISSN 10706631.
- [56] Hua Sheng Xie. PDRF: A general dispersion relation solver for magnetized multi-fluid plasma. *Comput. Phys. Commun.*, 185(2):670–675, 2014. ISSN 00104655.